Improved UTE-based attenuation correction for cranial PET-MR using dynamic magnetic field monitoring

A. P. Aitken, D. Giese, C. Tsoumpas, P. Schleyer, S. Kozerke,[a] C. Prieto,
and T. Schaeffter[b]
Department of Biomedical Engineering, Division of Imaging Sciences and Biomedical Engineering, King's College London, King's Health Partners, St. Thomas Hospital, London SE1 7EH, United Kingdom

(Received 26 March 2013; revised 30 October 2013; accepted for publication 18 November 2013; published 17 December 2013)

Purpose: Ultrashort echo time (UTE) MRI has been proposed as a way to produce segmented attenuation maps for PET, as it provides contrast between bone, air, and soft tissue. However, UTE sequences require samples to be acquired during rapidly changing gradient fields, which makes the resulting images prone to eddy current artifacts. In this work it is demonstrated that this can lead to misclassification of tissues in segmented attenuation maps (AC maps) and that these effects can be corrected for by measuring the true k-space trajectories using a magnetic field camera.
Methods: The k-space trajectories during a dual echo UTE sequence were measured using a dynamic magnetic field camera. UTE images were reconstructed using nominal trajectories and again using the measured trajectories. A numerical phantom was used to demonstrate the effect of reconstructing with incorrect trajectories. Images of an ovine leg phantom were reconstructed and segmented and the resulting attenuation maps were compared to a segmented map derived from a CT scan of the same phantom, using the Dice similarity measure. The feasibility of the proposed method was demonstrated in *in vivo* cranial imaging in five healthy volunteers. Simulated PET data were generated for one volunteer to show the impact of misclassifications on the PET reconstruction.
Results: Images of the numerical phantom exhibited blurring and edge artifacts on the bone–tissue and air–tissue interfaces when nominal k-space trajectories were used, leading to misclassification of soft tissue as bone and misclassification of bone as air. Images of the tissue phantom and the *in vivo* cranial images exhibited the same artifacts. The artifacts were greatly reduced when the measured trajectories were used. For the tissue phantom, the Dice coefficient for bone in MR relative to CT was 0.616 using the nominal trajectories and 0.814 using the measured trajectories. The Dice coefficients for soft tissue were 0.933 and 0.934 for the nominal and measured cases, respectively. For air the corresponding figures were 0.991 and 0.993. Compared to an unattenuated reference image, the mean error in simulated PET uptake in the brain was 9.16% when AC maps derived from nominal trajectories was used, with errors in the $\mathrm{SUV}_{\max}$ for simulated lesions in the range of 7.17%–12.19%. Corresponding figures when AC maps derived from measured trajectories were used were 0.34% (mean error) and −0.21% to +1.81% (lesions).
Conclusions: Eddy current artifacts in UTE imaging can be corrected for by measuring the true k-space trajectories during a calibration scan and using them in subsequent image reconstructions. This improves the accuracy of segmented PET attenuation maps derived from UTE sequences and subsequent PET reconstruction.
[http://dx.doi.org/10.1118/1.4837315]

Key words: Magnetic resonance imaging, positron emission tomography, attenuation correction, ultrashort echo time, eddy currents, artifacts, magnetic field monitoring

1. INTRODUCTION

The first whole-body hybrid PET-MR scanner has recently been introduced into clinical practice.[1] Such systems offer several advantages over PET/CT scanners, including improved soft tissue contrast and reduced radiation dose. The latter also provides the potential for motion compensated PET reconstruction to be performed.[2,3] However, deriving attenuation maps using hybrid PET-MR systems remains challenging.[4,5] Accurate attenuation correction (AC) is of great importance in PET, especially for lesions near bones.[6] In hybrid PET/CT systems, AC maps can be derived from CT images by scaling Hounsfield units (HU) to the equivalent attenuation coefficients at 511 keV.[7] However, deriving AC maps using MR imaging requires more sophisticated methods because no direct relationship exists between MR signal intensity and PET attenuation coefficients. In particular, cortical bone and air have low intensity in conventional MR sequences, but have very different attenuation coefficients in PET.

Several methods for producing AC maps from MRI have been proposed, which can be broadly categorized into *nonlinear registration-based* and *segmentation-based* methods. In nonlinear registration-based methods, an existing template AC map is transformed to match the anatomy of a new patient using a transform derived using nonlinear image registration.[8–12] The template AC map can be created using previously acquired CT (Refs. 8 and 12) or transmission scans[9–11] of one or more other subjects, or from a segmented tissue atlas.[11] In some cases the template AC map is paired with a coregistered template MR image.[8,9,11] The MR template image is then registered to the MR image of the new patient and the resulting transform is applied to the template AC map. In other cases, the registration is performed directly between the new MR images and the template AC map.[12]

In segmentation-based methods, each voxel is classified as a particular tissue type and subsequently assigned an appropriate attenuation coefficient based on typical values for that tissue.[13–18] Other recent methods have followed a similar approach to segmentation-based methods, but with the signal intensities from the MR images being used to assign continuous valued attenuation coefficients to each voxel,[8,19,20] rather than classifying each voxel and then assigning discrete values. Several methods also incorporate additional information such as the location of the voxel or the MR image intensities in neighboring voxels when assigning attenuation coefficients.[8,16,17,20] A combination of registration-based and segmentation-based methods can also be used.[8]

Accurately assigning attenuation coefficients to bone using MR images is challenging because cortical bone exhibits low proton densities and very fast transverse relaxation rates (T_2^*), causing it to appear with low intensities with standard MRI pulse sequences, which do not begin sampling until the signal has decayed substantially.[21] This makes it difficult to distinguish cortical bone from air, making it challenging to segment bone accurately and impossible to convert the MR signal intensity directly to the appropriate Hounsfield units.

A potential solution is to perform direct sampling of the free induction decay (FID) immediately after radiofrequency (RF) excitation using ultrashort echo time (UTE) sequences, such as the one depicted in Fig. 1, so that the short-lived signal from bone can be sampled.[14,15,20] To help further distinguish cortical bone from soft tissue, the FID readout can be followed by a gradient echo to produce a second image in which only signal from soft tissue remains. Taking the natural logarithm of the FID and echo images and then performing a subtraction yield a scaled map of the transverse relaxation rate ($R_2^* = 1/T_2^*$) in each voxel, in which cortical bone appears with high intensity and soft tissue appears with low intensity. The acquired images and the derived R_2^* map can then be used to produce a segmented AC map,[15] or a regression model can be used on the acquired images to derive pseudo-CT based AC maps.[19,20]

It still remains challenging to accurately derive attenuation maps from UTE sequences in regions containing boundaries between air and soft tissue or between bone and soft tissue. Boundaries between air and tissue often appear with high intensities in R_2^* maps or subtraction images derived from multiecho sequences, leading to misclassifications in segmented AC maps,[15] or errors in pseudo-CT images.[19] These hyperintensities have been attributed to collagen content in skin,[15] which also has high R_2^* values and to susceptibility differences between different tissue types,[19] which increase the R_2^* values in these regions.

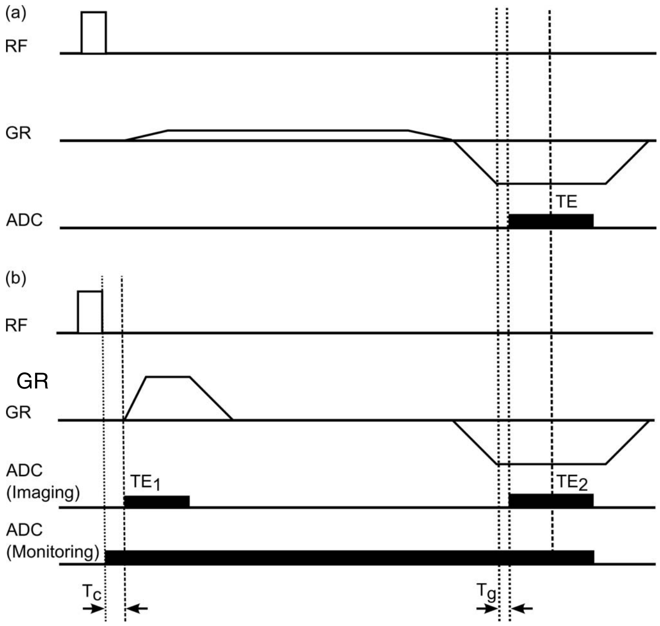

FIG. 1. Pulse sequence timing diagrams for (a) gradient echo sequence with echo time TE and (b) dual echo UTE sequence with an FID readout beginning at time TE$_1$, followed by a gradient echo readout at time TE$_2$ = TE. "RF" and "GR" represent the radiofrequency and gradient fields, respectively. "ADC" represents the readout timings (analog to digital conversion). In both sequences, time T$_g$ represents the delay between reaching the plateau of the gradient waveform and the start of the echo readout. This delay is employed to allow the field to settle before the readout begins. For the UTE sequence, time T$_c$ represents the delay between RF excitation and the start of the readout due to tuning of the RF coil. Note that the FID readout in the UTE sequence begins while the gradient fields are ramped at high slew rates and then continues after the flat part of the gradient waveform is reached.

When the gradient fields are ramped up during a MRI sequence, the change in the magnetic field induces eddy currents in the gradient coils and nearby conductors, which in turn produce a field that opposes the original change in the field strength. This leads to deviations between the desired k-space trajectories (sampling positions) and those realized by the scanner, leading to degradation of the reconstructed images.[22] System latencies also lead to timing errors, which cause the k-space trajectories to be shifted, leading to further artifacts.

Although the effects of eddy currents and delays can be corrected for in part by use of gradient pre-emphasis, and by shifting and scaling the k-space trajectories prior to reconstruction,[13] it is common for some residual effects to occur even for an optimally configured system (results of simulations in which these effects are demonstrated are shown in Figs. S1–S3 of the supplementary material.[43] This is especially true for eddy currents that decay with short time constants.[23] The influence of eddy currents on the reconstructed image depends on the sampling trajectory, the timing of the sequence and on the rate at which the gradient fields are ramped up (the "slew rate"). These effects are particularly prominent in UTE imaging because the acquisition must begin immediately after excitation, while the field gradients are ramping with high slew rates,[23] whereas in conventional imaging the readout is performed on the plateau of the gradient waveform, after a short delay to allow the field to settle before the acquisition, as shown in Fig. 1. Pre-emphasis waveforms are generally designed to minimize errors when sampling is performed during the plateau of the gradient waveform, rather than for the special case of ramp sampling. UTE imaging is therefore more susceptible to errors introduced by short term eddy current behavior that are not corrected for by pre-emphasis.[23] Finally, projection based phase corrections can be applied to data that are acquired using conventional radial sampling schemes[24] to reduce the effects of k-space trajectory deviations, but similar methods have yet to be developed for UTE imaging, in which only half of a projection is acquired during each repeat of the sequence. The aforementioned differences between UTE imaging and conventional gradient echo imaging are particularly important when using an FID image and a subsequent echo image to estimate R_2^* maps, because any differences between the two images due to artifacts will lead to errors in estimates of the R_2^* values.

Dynamic magnetic field monitoring[25,26] using a field camera has recently been proposed as a way to account for eddy current effects in several applications.[27,28] The true k-space trajectories are measured during a separate calibration scan, allowing both short and long term eddy current behavior to be measured. These effects can then be accounted for by using the measured trajectories in standard MRI gridding reconstruction algorithms in place of the nominal trajectories. In this work it is shown that system delays and eddy current effects contribute substantially to errors in UTE derived attenuation maps, by introducing blurring and edge artifacts in the UTE images, especially at the interfaces between bone and soft tissue and between soft tissue and air. It is also demonstrated that these artifacts can be corrected for by measuring the true k-space trajectories using a magnetic field camera. This leads to improved classification of bone in segmented attenuation maps for use in PET. However, the proposed correction method is not limited to the particular pulse sequence used and could be applied to other similar methods[13–16,19,20] for generating attenuation maps using UTE. A numerical phantom is used to demonstrate the effects of complex deviations in k-space on the image reconstruction and of subsequent correction using a field camera. Correction of eddy current artifacts using the field camera is then demonstrated using an ovine leg tissue phantom and subsequently for *in vivo* cranial imaging of five healthy volunteers. PET simulations using attenuation maps derived using nominal and measured k-space are presented for one volunteer.

2. MATERIALS AND METHODS

2.A. UTE sequence and MR-based attenuation maps

Segmented attenuation maps were derived from MRI based on the method proposed by Keereman *et al.*[15] In this method, 3D radial ("koosh-ball") dual-echo UTE scans are acquired, in which sampling of the FID at time TE_1 is followed by sampling of a gradient echo at time TE_2, to produce images I_1 and I_2, respectively, as shown in Fig. 1(b). The radial k-space trajectories as a function of time during a single repetition of the pulse sequence are shown in Fig. 2(b). The FID readout begins as the gradients are ramped up, giving an initially quadratic k-space trajectory, which becomes linear after the gradient plateau is reached. The gradient echo is acquired entirely during a gradient plateau and so the trajectory is linear throughout the second acquisition.

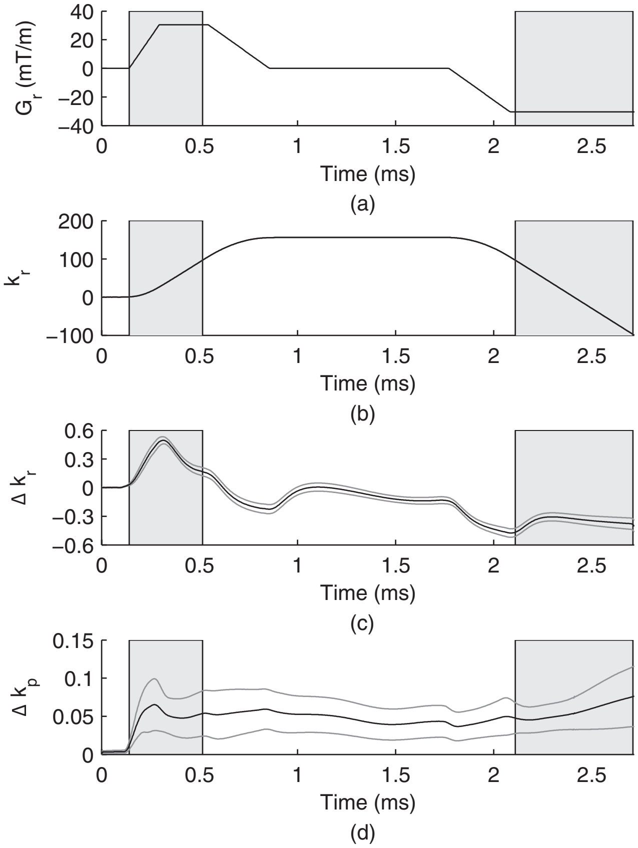

FIG. 2. (a) Dual echo UTE gradient waveform (G_r) as a function of time after RF excitation. Gray bands delineate the sampling periods for the FID readout (TE = 0.14 ms) and for the gradient echo readout (TE = 2.41 ms). (b) Nominal k-space trajectory along the direction parallel to an arbitrary spoke (k_r) (normalized to the nominal field of view). (c) Error between the measured and nominal trajectory along the spoke direction (Δk_r). (d) Magnitude of the error between the measured and nominal trajectories in the plane perpendicular to the spoke (Δk_p). (c) and (d) The black lines represent the mean error across all spokes and the gray lines show ± one standard deviation.

To produce a segmented AC map, I_1 is first thresholded to segment air from soft tissue and cortical bone. An R_2^* map is then calculated as

$$R_2^* = \frac{\ln I_2 - \ln I_1}{TE_1 - TE_2}. \tag{1}$$

The air segmentation is then used to mask out air in the R_2^* map. Finally, the masked R_2^* map is thresholded to segment cortical bone and soft tissue. Appropriate attenuation coefficients are then assigned to each segment.

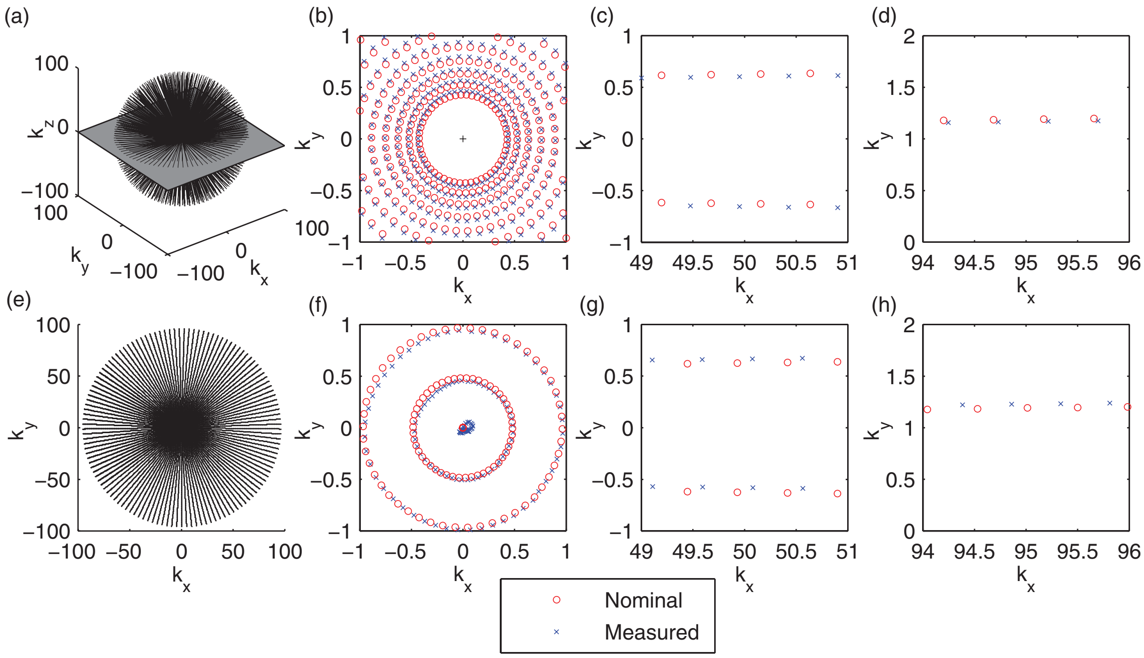

FIG. 3. Nominal and measured k-space trajectories for 3D radial UTE scan (normalized to the nominal field of view). (a) and (e) Several spokes from the 3D readout (a) are projected onto the k_x–k_y plane (e). (b) and (f) Zoomed region in k-space center for FID (b) and echo (f). Due to the high sampling density in the center of k-space for the FID readout, every second radial sampling point is omitted in (b) to aid visualization. (c) and (g) Zoomed region approximately half way between center and edge of k-space for FID (c) and echo (g). (d) and (h) Zoomed region at outer edge of k-space for FID (d) and echo (h).

All images were acquired on a 3 T system (Achieva TX, Philips Medical Systems, Best, The Netherlands) with a 3D "koosh-ball" radial trajectory using an eight channel head coil. The koosh-ball sequence consisted of several k-space "spokes," each of which was acquired during a single excitation and corresponds to one FID/echo readout pair. Each spoke was rotated relative to the previous so that the outer points of the spoke cover the surface of a sphere, as shown in Fig. 3(a). The following sequence parameters were used: $\mathrm{TE}_1/\mathrm{TE}_2 = 0.14/2.41$ ms, repetition time = 4.7 ms, flip angle = 10°, field of view = 250 mm diameter, and voxel size = 1.25 mm isotropic.

For the ovine phantom scans, fully sampled k-space data were acquired, such that the Nyquist criterion was fulfilled in both the radial and angular directions, giving a scan time of 7 min 32 s. The numerical phantom data were simulated with the same sampling pattern as the ovine phantom. In both cases reconstruction was performed using a nonuniform fast Fourier transform,[29] with a correction for the sample density computed using an iterative method.[30] For the *in vivo* scans, angular undersampling by a factor of 4 was employed to reduce the scan time to 1 min 45 s. To avoid undersampling artifacts in these images, reconstruction was performed using a self-calibrating[31] non-Cartesian parallel imaging technique.[32]

2.B. Dynamic magnetic field monitoring

A dynamic magnetic field camera[25] (Skope Magnetic Resonance Technologies LLC, Zurich, Switzerland) was used to measure the magnetic field evolution during UTE scans. The camera head consists of 16 transmit/receive NMR probes[33] arranged on the surface of a sphere, as shown in Fig. 4. Prior to the main monitoring experiment, four calibration measurements are made to determine the Larmor frequencies and positions of the probes within the scanner. Each measurement consists of a radiofrequency (RF) excitation followed by sampling of the FID, either in the presence of no gradients (to determine Larmor frequencies) or in the presence of a gradient in one of three orthogonal directions (to determine the *x*, *y*, and *z* positions). For the main monitoring experiment, the UTE pulse sequence is played out as usual, with the probes being excited on every repetition of the sequence. Sampling

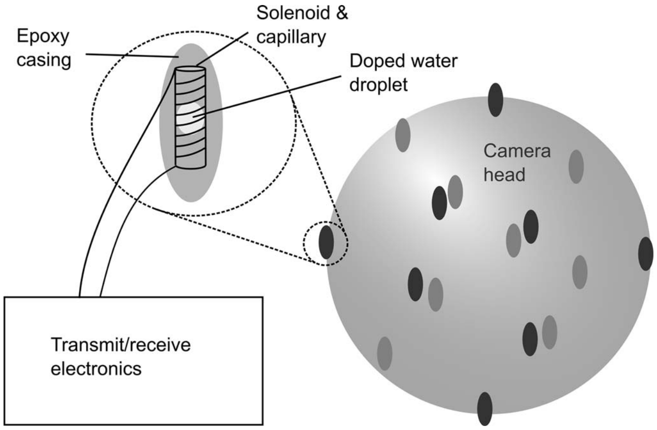

FIG. 4. Schematic diagram of dynamic magnetic field camera (Skope Magnetic Resonance Technologies, Zurich, Switzerland). Sixteen transmit/receive NMR probes are mounted on the surface of a sphere. The phase evolution of each probe is recorded during a calibration scan in which the pulse sequence of interest is played out. The phase and known positions of each probe are used to calculate the coefficients of a field model as a function of time. The true k-space trajectories and B_0 field evolution are extracted from the model and used in image reconstruction.

occurs continually throughout each repetition, rather than being split into two as is the case during imaging (for FID and echo sampling), as shown in Fig. 1(b).

The phase of the signal from a particular probe is related to the history of the local field strength surrounding that probe. As the position and Larmor frequency of each probe is known from the calibration measurements, the phase of the signal measured during the UTE monitoring scan can be used to fit a model to the field using an expansion of spherical harmonics. This is done by solving for the coefficients k_l in the following equation:[25]

$$\phi_j(t) = \gamma B_{\mathrm{ref}\,j}\, t + \sum_{l=1}^{N_l} k_l(t) f_l(\boldsymbol{r}_j), \tag{2}$$

where $\phi_j(t)$ is the measured phase from the jth probe at position $\boldsymbol{r}_j$ at time t, γ is the gyromagnetic ratio for water, $B_{\mathrm{ref}\,j}$ is the local field strength in a reference state (determined from the probes' Larmor frequencies), and f_l is the lth of N_l spherical harmonic basis functions described with dynamic coefficients k_l. With 16 probes, up to 16 coefficients can be determined, allowing an expansion in the spherical harmonic basis up to the third order. For standard Fourier-based image reconstruction, only terms up to the first order are required, which correspond to dynamic measurement of drift of the main magnetic field (B_0) strength (zeroth order term) and measurement of k-space trajectories (first order terms). In principle, higher order terms can be incorporated into the reconstruction by solving the forward signal equation using an iterative method.[27] However, this requires a specialist reconstruction algorithm and leads to a substantial increase in reconstruction time. Therefore, only first order reconstruction is performed in this work. All data processing and reconstruction were performed in MATLAB (R2012b, The Mathworks, Natick, MA), with parts of the pipeline utilizing the ReconFrame package (Gyrotools LLC, Zurich, Switzerland).

2.C. Experiments

2.C.1. Trajectory measurement

To measure the true k-space trajectories during the FID and echo readouts, a separate field monitoring scan was performed as a calibration step prior to imaging. The same scan parameters were used for both field monitoring and imaging, with the exception of the flip angle, which was set to 90° during the monitoring scan to maximize the signal strength, the readout period, which was stretched along the entire repetition time in order to track the phase evolution throughout, and the repetition time, which was increased to 100 ms for the monitoring experiment to avoid saturation of the signal from the field camera probes.

2.C.2. UTE simulations

As predicting the effect of complex k-space trajectory deviations on image reconstruction is challenging, a numerical phantom was used to demonstrate the appearance of artifacts in UTE images when reconstruction is performed using nominally calculated k-space trajectories, rather than the true trajectories. The phantom consists of three ellipsoids of different intensities, which when summed represent a long bone surrounded by soft tissue (soft tissue intensity = 1/0.98, bone intensity = 0.2/0.03 for FID/echo, respectively), as shown in Fig. 5. k-space data for the phantom were simulated for the FID and echo acquisitions by analytically evaluating the Fourier transform of the three ellipses at the points corresponding to the k-space trajectories measured using the field camera. The simulated k-space data were then used to reconstruct images first using the nominal trajectories and separately using the trajectories measured using the field camera. For the nominal echo image, absolute and linear phase corrections were applied.[24] Segmented attenuation maps were then derived from the resulting images and R_2^* maps. For comparison, "ground truth" segmentations were generated by evaluating the ellipse equations in image space. The segmentations derived from the reconstructed images were compared to the true segmentations using the Dice similarity coefficient.[34]

2.C.3. Tissue phantom imaging

UTE images were acquired of an ovine leg phantom. Images were reconstructed in the same manner as for the simulated data, with an additional correction for temporal B_0 changes performed in the measured case, using the measured zeroth order coefficients. CT images were acquired of the phantom for comparison, using a combined PET/CT scanner (Discovery VCT, GE Healthcare, Waukesha, WI) with the following parameters: 140 kVp, 350 mAs, in plane voxel size = 1.3 mm, slice thickness = 1.25 mm, pitch = 0.53. CT images were registered to the FID UTE images using rigid registration[35] with normalized cross correlation as the similarity measure. CT images were segmented using intensity based thresholding on HU. As the UTE sequence provides contrast between cortical bone and soft tissue but not between trabecular bone and soft tissue, thresholds were chosen to separate cortical bone (HU $>$ 800), soft tissue ($-200 <$ HU < 800) and air (HU < -200). The threshold between air and soft tissue was also effective in classifying the plastic container surrounding the phantom as air. The accuracy of the bone segmentation in the MR-derived attenuation maps was assessed for a volume of interest covering 50 central slices using the Dice similarity coefficient.

2.C.4. in vivo imaging

Cranial UTE images of five healthy volunteers were acquired following provision of informed consent. To avoid unnecessary radiation dose to the volunteers, CT scans were not acquired for comparison and so the images and resulting segmentations were evaluated qualitatively.

2.C.5. PET simulations

PET simulations were performed for one volunteer to demonstrate the effect of misclassifications in the attenuation map due to eddy currents on the PET reconstruction, as illustrated in Fig. 6. An emission map containing bone, air, and

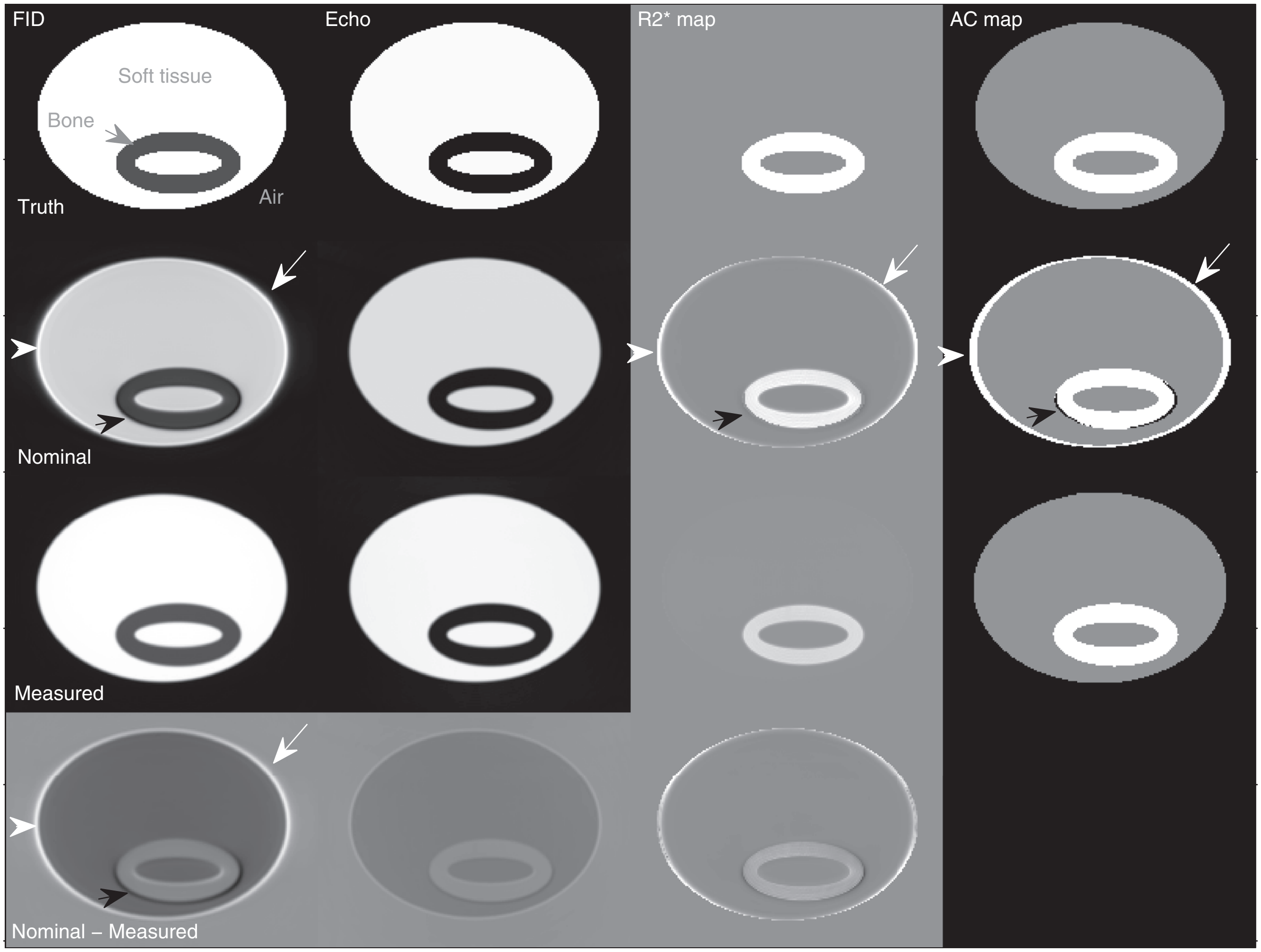

FIG. 5. Simulated UTE images of a long bone surrounded by soft tissue. k-space data were generated by evaluating the Fourier transform of the ellipses forming the phantom at the locations given by the trajectories measured using the field camera. Images were then reconstructed using the nominal k-space trajectories and again using measured trajectories. Prominent hyperintense edge artifacts are seen on the air–tissue border in the FID images reconstructed with the nominal trajectories (white arrows), as well as hypointense bands on the bone–soft tissue border (black arrows). The former leads to misclassification of soft tissue as bone in the attenuation map and the latter leads to misclassification of bone as air. In addition, there is blurring in the FID images reconstructed with nominal trajectories (short white arrow), which leads to air being misclassified as bone.

soft tissue regions was generated from the segmentations derived using the measured trajectories. To add contrast in the emission map between gray matter, white matter, and CSF, the BrainWeb[36] tissue atlas was transformed into the same space as the MR images of the volunteer based on affine registration[35] between the Brainweb proton density MRI template and the echo image from the volunteer dataset. The voxels in the emission map corresponding to gray matter, white matter, and CSF in the transformed atlas were then reclassified accordingly. Three artificial spherical tumors of diameter 20 mm were then placed in various locations: (1) in the center of the brain; (2) at the posterior of the brain close to the skull; and (3) posterior the nasal sinuses. The following emission values, representing typical standardized uptake values (SUV) were assigned to each tissue: tumor = 6, gray matter = 2.7, white matter/other soft tissue = 1, bone = 0.3, and CSF = 0.

Fully three dimensional (3D) simulated PET data were then produced using an approach based on the method described by Tsoumpas *et al.*[37] A reference sinogram was derived by forward projection of the emission map. An attenuated sinogram was generated from the reference sinogram by applying the corresponding attenuation coefficient factors (ACFs) calculated from the attenuation map derived using measured trajectories. Fully 3D scatter was also estimated from the emission and attenuation maps derived using measured trajectories as described by Tsoumpas *et al.*[38] The scatter was then added to the attenuated sinogram. The reference sinogram and the attenuated sinogram with scatter were then scaled to simulate 10 min, fully 3D FDG acquisitions (100×10^6 counts without scatter and 150×10^6 counts including scatter). Poisson noise was then added to each of the two sinograms.

OSEM iterative reconstruction was performed using the STIR package[39] with the following parameters: 2 iterations, 28 subsets, matrix size = 128 × 128 × 23, voxel size = $2 \times 2 \times 3.27$ mm^3, 4 mm full-width at half-maximum Gaussian postprocessing filter. A reference PET image (PET$_{\text{ref}}$)

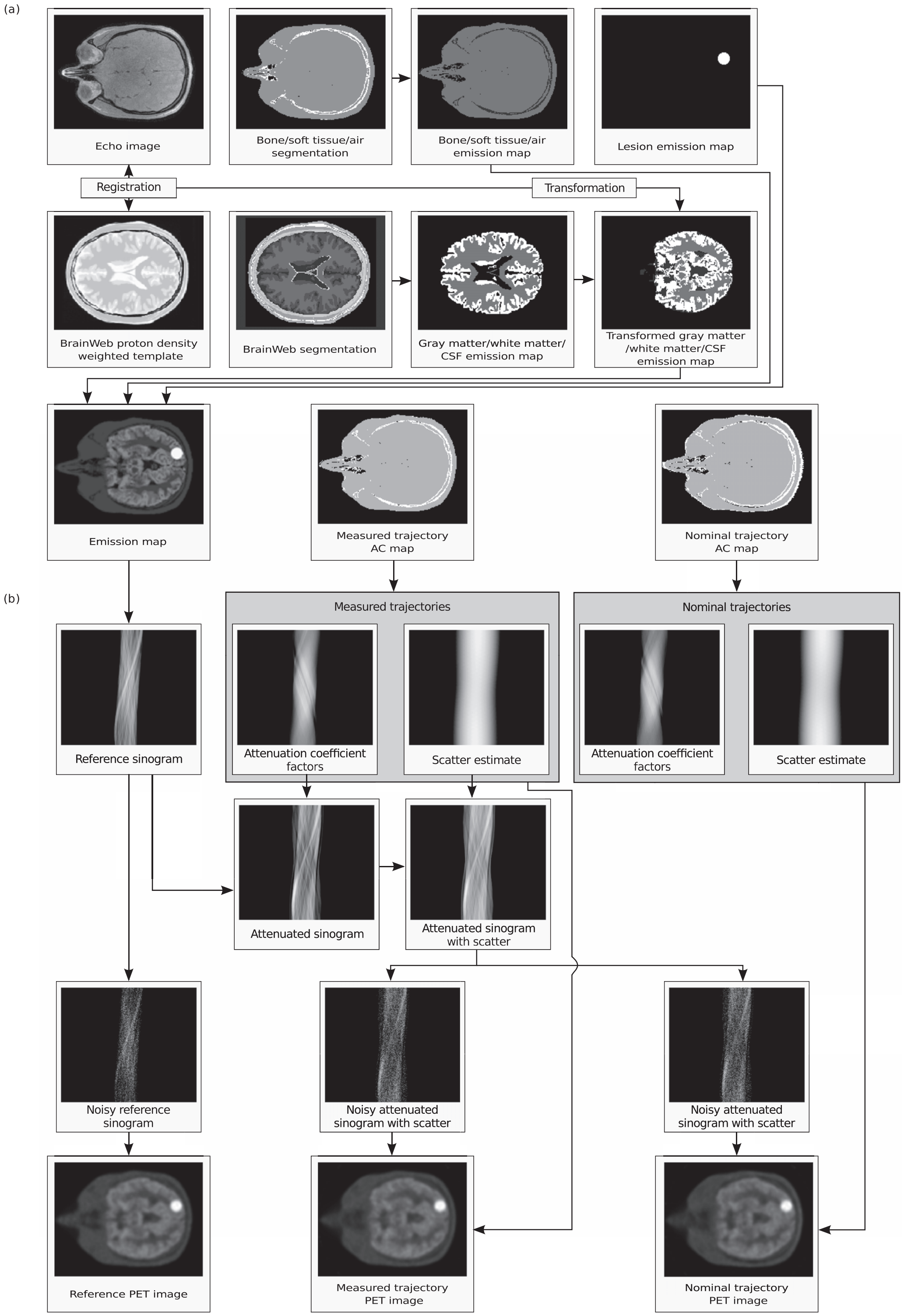

FIG. 6. Generation of simulated emission map: The segmentation derived from the images reconstructed using measured trajectories was used to generate an emission map containing bone, air, and soft tissue. The BrainWeb proton density weighted template was then registered to the echo image that was reconstructed with measured trajectories. Gray matter, white matter, and cerebrospinal fluid were extracted from the brain web segmented atlas, and typical emission values were assigned to each of these three tissue types to produce a brain emission map. The brain emission map was transformed using the affine matrix that was derived from the registration and was then combined with the bone/soft/tissue/air emission map before the addition of spherical lesions. The combined segmented emission map was then smoothed with a Gaussian filter and down-sampled. PET simulation pipeline: The simulated emission map was forward-projected to produce a reference sinogram. The attenuation maps derived using measured trajectories were used to calculate the ACFs and scatter component. The ACFs were then multiplied with the reference sinogram before addition of the scatter estimate, to produce an attenuated sinogram with scatter. Poisson noise was added to the reference sinogram and to the attenuated sinogram with scatter. A reference PET image ($\mathrm{PET_{ref}}$) was reconstructed from the noisy reference sinogram, without simulating or correcting for attenuation or scatter in the reconstruction. The noisy attenuated sinograms with scatter were reconstructed in one case using the scatter estimate and ACFs derived from the measured trajectories ($\mathrm{PET_{meas}}$), and in a second case using ACFs and a scatter estimate derived from nominal trajectories ($\mathrm{PET_{nom}}$).

was reconstructed from the reference sinogram without simulation and consecutive corrections for attenuation and scatter effects. This provided an ideally reconstructed reference image with no influence from any errors due to attenuation or scatter. The attenuated sinogram data with scatter were reconstructed using within the algorithm the attenuation correction factors and scatter estimates derived using both the nominal and measured trajectories, to give images denoted $\mathrm{PET_{nom}}$ and $\mathrm{PET_{meas}}$, respectively. Differences in the maximum and mean SUV ($\mathrm{SUV_{max}}$ and $\mathrm{SUV_{mean}}$) were calculated for each tumor relative to $\mathrm{PET_{ref}}$ using regions of interests defined by the original extent of each tumor in the emission map.

3. RESULTS

3.A. Trajectory measurements

Figures 2(c) and 2(d) show the mean deviations across all spokes between the measured and nominal trajectories as a function of time t after excitation. Figure 2(c) shows the deviations in the direction parallel to the spoke (Δk_r). Both short and long term effects are evident. The deviations during the FID readout are dominated by short term effects; there is a rapid increase in the size of the deviation during ramping of the gradients, which decays quickly as the plateau is reached. The deviations during the echo readout are dominated by long term effects, leading to a relatively constant parallel shift of the trajectory across the readout, with the exception of a short lived component at the beginning of the readout, which occurs as a result of ramping of the gradients before the readout. Figure 2(d) shows the magnitude of the deviations in the plane that is perpendicular to the spoke direction (k_p) and contains the current nominal sampling point at t. The nominal and measured trajectories diverge rapidly at the beginning of the FID readout and then the size of the deviation remains relatively constant before rising again slowly throughout the echo readout.

The nominal and measured trajectories are shown for several spokes in Fig. 3. To aid visualization, the trajectories are projected onto the k_x–k_y plane [Figs. 3(a) and 3(e)]. Several zoomed regions are also shown. Figures 3(b)–3(d) show zoomed regions for the FID readout in the center of k-space [Fig. 3(b)], where the errors are small; approximately halfway between the center and edge of k-space [Fig. 3(c)], where the short term eddy current effects have their maximum effect; and finally at the edge of k-space [Fig. 3(d)], where the deviations are again small. It is clear from Fig. 3(b) that the deviations are anisotropic across k-space.

Equivalent regions for the echo readout are shown in Figs. 3(f)–3(h). Figure 2(d) shows that there is a shift along the direction parallel to the spoke throughout the entire k-space during the echo readout, which is commonly corrected for using projection based linear phase correction.[24] In this correction, the parallel shifts of opposing k-space spokes are estimated from the linear phases of the associated projections. The calculated linear phase is then subtracted from the data before gridding, or equivalently the k-space trajectories can be shifted accordingly. As this correction is routinely applied in radial gradient echo imaging, the results shown in Figs. 3(f)–3(h) reflect the trajectories after the application of this correction, with the linear phases estimated from the simulated phantom data. After this correction, the errors in the k-space center [Fig. 3(f)] are small (<0.1). It is again clear that the eddy current effects are anisotropic across k-space. The residual parallel shifts in Figs. 3(g) and 3(h) are of similar size to each other (approximately 0.25) but of opposite sign and are due to short term effects following ramping of the gradients.

3.B. UTE simulations

In order to assess the effect of k-space trajectory deviations on the reconstructed images, simulated UTE images reconstructed with nominal and with measured k-space trajectories are shown in Fig. 5. For comparison, the true images generated using the image space ellipse equations are also shown, along with the corresponding segmentation. The FID images reconstructed with nominal trajectories exhibit hyperintense edge artifacts (white arrows) and blurring (short white arrows) on the air–tissue border and hypointense artifacts on the border between bone and soft tissue (black arrows). The hyperintensities lead to misclassification of soft tissue as bone; blurring leads to misclassification of air as bone and the hypointensities lead to misclassification of bone as air. None of these artifacts appear in the images reconstructed with measured trajectories. The Dice coefficients between the bone segmentations derived from the reconstructed images and the true bone segmentation were 0.993 and 0.410 for the images reconstructed with measured and nominal trajectories, respectively. For soft tissue the corresponding figures were 0.978 and 0.973 and for air they were 0.994 and 0.974.

3.C. Tissue phantom imaging

UTE images of the tissue phantom reconstructed with nominal and with measured k-space trajectories are shown in Fig. 7, along with calculated R_2^* maps and segmented attenuation maps for each case. Difference images between nominal and measured cases are also shown, along with a CT image of the same slice for comparison. The difference images highlight edge artifacts in the images reconstructed with nominal trajectories, which are more prominent in the FID images than in the echo images, and follow a similar pattern to those in the simulated data. The artifacts manifest in the R_2^* maps as a hyperintense ring on the air–tissue border (white arrows), as well as a hypointense line on the bone–tissue border (black arrows). The hyperintensities again lead to misclassification of both air and soft tissue as bone and the hypointensities lead to misclassification of bone as air. These artifacts are greatly reduced in the R_2^* map derived from the images reconstructed with measured trajectories, as is the ring of misclassified bone in the attenuation map. Dice coefficients for bone in MR relative to CT were 0.814 and 0.616 for AC maps derived using the measured and nominal trajectories, respectively. For soft tissue, the corresponding figures were 0.934 and 0.933 and for air they were 0.993 and 0.991.

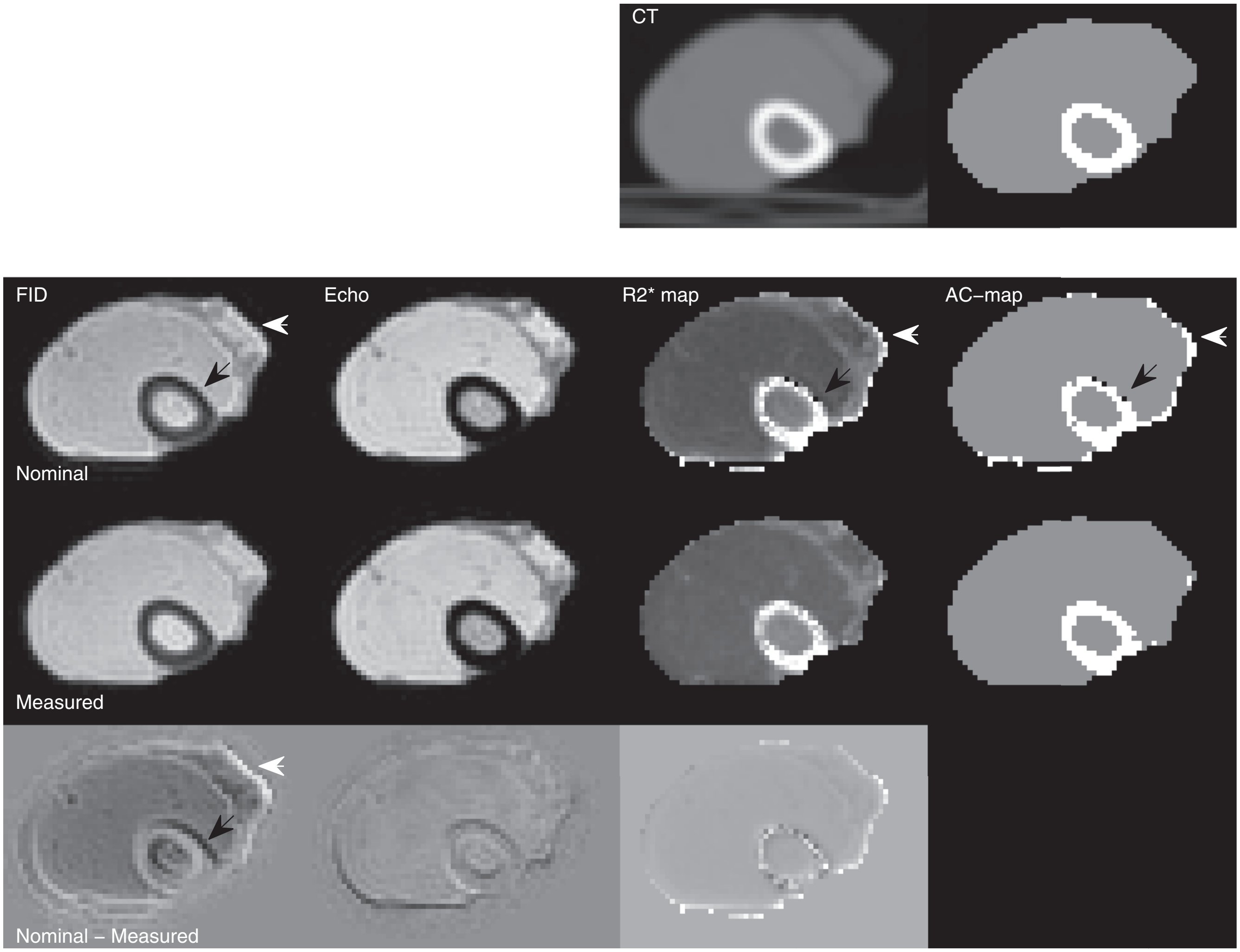

FIG. 7. UTE-MR and CT images of an ovine leg phantom. Top row: Reference CT image and segmented attenuation map derived from CT. Second row: UTE-MR images reconstructed using nominal k-space trajectories, with corresponding R_2^* map and segmented AC maps. Third row: As second row but with images reconstructed using k-space trajectories measured with a field camera. Fourth row: Differences between images reconstructed with nominal trajectories and with measured trajectories. Black arrows show hypointense artifacts on the bone–soft tissue border, leading to misclassification of bone as air. White arrows show hyperintense artifacts on the air–soft tissue border, leading to misclassification of soft tissue as bone.

3.D. *in vivo* imaging

Typical *in vivo* images are shown in Fig. 8. As with the tissue phantom and simulations, hyperintense edge artifacts are seen on the air–tissue border in the images reconstructed with nominal trajectories, leading to a layer of bone appearing on the outer edge of the head in the attenuation map (white arrows). This is removed when the images are reconstructed with measured trajectories. Hypointense areas in the skull in the nominal FID images also lead to misclassification of bone as air (black arrows), which are corrected for in the images reconstructed with measured trajectories. Axial, sagittal, and coronal slices of the R_2^* maps and AC maps from a second volunteer are shown in Fig. 9. Again the layer of misclassified bone on the skin is apparent in the AC maps derived using the nominal trajectories, which is corrected for when the measured trajectories are used. There are no visible streaking artifacts due to undersampling.

3.E. PET simulations

Reconstructed PET images ($\mathrm{PET}_{\mathrm{ref}}$) for the three slices containing the simulated tumors are shown superimposed on the MR echo images in Fig. 10. Relative differences between $\mathrm{PET}_{\mathrm{nom}}$ and $\mathrm{PET}_{\mathrm{ref}}$, between $\mathrm{PET}_{\mathrm{meas}}$ and $\mathrm{PET}_{\mathrm{ref}}$, and between $\mathrm{PET}_{\mathrm{nom}}$ and $\mathrm{PET}_{\mathrm{meas}}$ are also shown. To remove background signal and to aid visualization of the brain, the difference maps were masked based on the union of the gray matter, white matter, and CSF BrainWeb masks. In general, uptake was overestimated in $\mathrm{PET}_{\mathrm{nom}}$, with a mean relative difference in the brain of 9.16% between $\mathrm{PET}_{\mathrm{nom}}$ and $\mathrm{PET}_{\mathrm{ref}}$. The corresponding figure between $\mathrm{PET}_{\mathrm{meas}}$ and $\mathrm{PET}_{\mathrm{ref}}$ was 0.34%. The largest errors in $\mathrm{PET}_{\mathrm{nom}}$ occurred in the posterior and superior regions of the brain, where large regions of misclassified bone appear in the attenuation maps. In these regions the relative difference tended to approximately 25% toward the inner surface of the skull. For the simulated lesions, relative

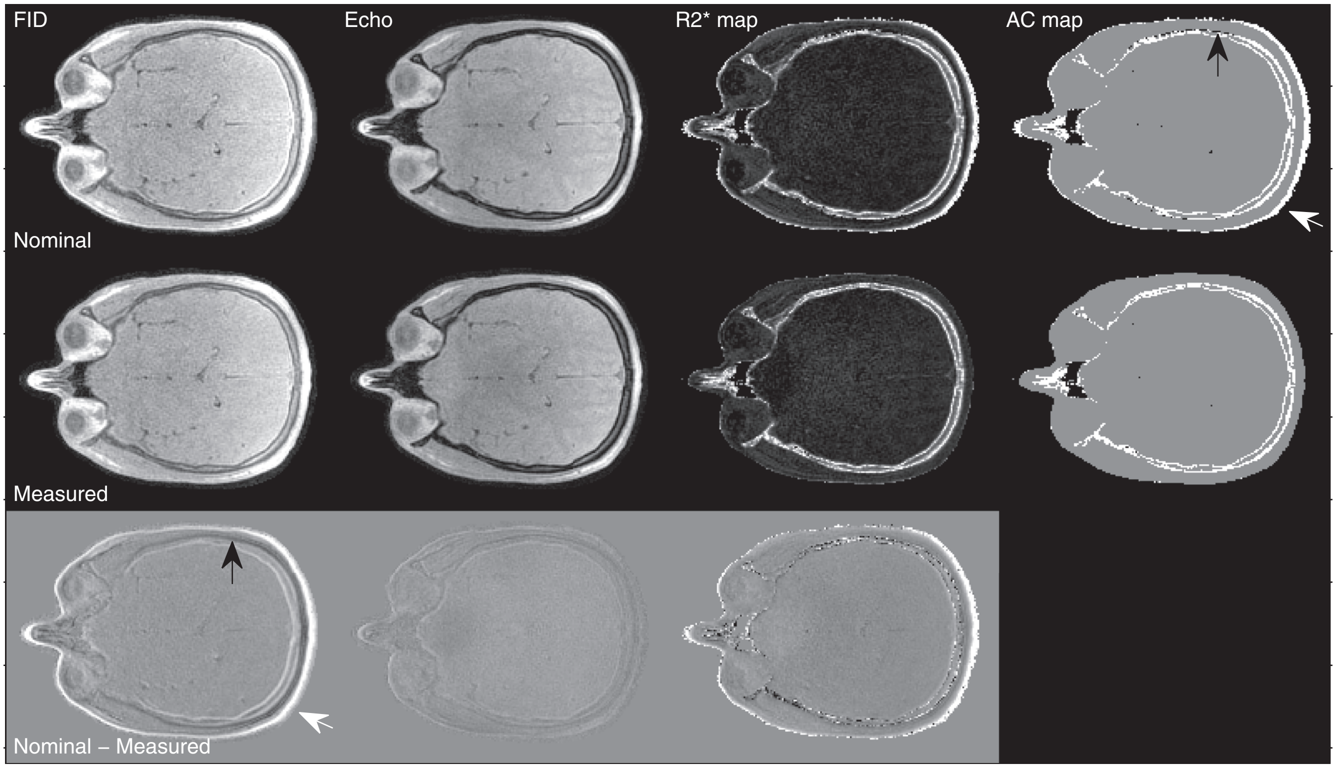

FIG. 8. UTE-MR images of the head of a volunteer. Top row: FID and echo images reconstructed with nominal k-space trajectories and corresponding R_2^* and segmented attenuation map. Middle row: As top row but with reconstruction performed with k-space trajectories measured with a field camera. Bottom row: Differences between images reconstructed with nominal trajectories and with measured trajectories. Black arrows show hypointense artifacts on the bone–soft tissue border, leading to misclassification of bone as air. White arrows show hyperintense artifacts on the air–soft tissue border, leading to misclassification of soft tissue as bone.

differences in $\mathrm{SUV}_{\mathrm{max}}$ between $\mathrm{PET}_{\mathrm{nom}}$ and $\mathrm{PET}_{\mathrm{ref}}$ were 7.17%, 10.51%, and 12.19%. Corresponding figures for $\mathrm{PET}_{\mathrm{meas}}$ were −0.21%, 1.11%, and 1.81%. For $\mathrm{SUV}_{\mathrm{mean}}$, corresponding differences were 4.15%, 11.13%, and 10.25% for $\mathrm{PET}_{\mathrm{nom}}$ and −2.13%, 0.86%, and −0.46% for $\mathrm{PET}_{\mathrm{meas}}$.

4. DISCUSSION

It has been demonstrated in this work that eddy current artifacts can lead to errors in PET attenuation maps derived from UTE MRI sequences and that these effects can be corrected for by measuring the true k-space trajectories with a magnetic field camera, which can then be used in the reconstruction in place of the nominal k-space trajectories. Simulation results demonstrate the introduction of artifacts when the nominal k-space trajectories are used in image reconstruction. Imaging of a tissue phantom and *in vivo* cranial imaging show that these artifacts are reduced when the measured k-space trajectories are used in the reconstruction.

Segmented attenuation maps derived from the phantom images were quantitatively compared to those derived from CT and an improvement in the accuracy of bone segmentation was observed when the measured trajectories were used instead of the nominal trajectories. The main improvements were due to the reduction of hyperintense artifacts on the edge of the phantom in the FID images, which lead to misclassification of soft tissue as bone in the nominal AC maps and also due to a reduction in blurring on the edge of the phantom that leads to misclassification of air as bone in the nominal AC maps. Furthermore, in the AC maps derived using nominal k-space trajectories, small regions of bone are misclassified as air due to hypointense edge artifacts on the bone–soft tissue interface in the FID image. Again, these were corrected for when the measured trajectories are used.

Despite improvements in the accuracy of the bone segmentation when measured trajectories are used in the reconstruction, some errors still occur compared to segmented maps derived from CT. Sources of error in UTE-derived attenuation maps have been investigated by Johansson *et al.*,[40] who discuss limitations of both segmentation based methods and methods involving continuous mappings of MR image intensities to HU. A limitation of current segmentation based methods is that a single bone class cannot account for the wide range of densities present across different types of bone. Methods involving a continuous mapping between MR and HU aim to address this problem, but large uncertainties (200–300 HU) still exist in bone regions.[40]

UTE sequences were proposed for PET/MR to help to distinguish between cortical bone and air. However, separation of trabecular bone from soft tissue using UTE remains challenging because the short T_2^* collagen component of the trabecular bone is masked by the long T_2 components of the marrow. Therefore, while it is relatively easy to adjust thresholds in CT to segment parts of the bone with different densities, this

FIG. 9. Axial, sagittal, and coronal slices from 3D R_2^* maps and segmented AC maps derived from cranial UTE MRI scans of a second volunteer reconstructed using nominal k-space trajectories and again with measured trajectories. Black arrows show hypointense artifacts on the bone–soft tissue border, leading to misclassification of bone as air in nominal AC maps. White arrows show hyperintense artifacts on the air–soft tissue border, leading to misclassification of soft tissue as bone in nominal AC maps.

is rather more challenging in MR. This makes the assessment of MR based segmentations relatively sensitive to the choice of thresholds. However, we found that over a wide range of thresholds, the segmented AC maps derived using measured trajectories had consistently higher Dice coefficients relative to CT compared to those derived using nominal trajectories. Furthermore, although UTE sequences help to distinguish between air and cortical bone, accurate segmentation is still challenging because cortical bone still has relatively low signal intensity and because the FID sampling scheme only covers half of a radial k-space spoke per excitation, leading to a relatively low signal to noise ratio.

In a previous study, Johansson *et al.*[19] introduced a method to reduce errors on the air–soft tissue and bone–soft-tissue interfaces that occur due to susceptibility differences between these tissues. They use a second UTE sequence with a different flip angle to help provide additional information about the longitudinal relaxation rate (T_1) in these regions. Despite these improvements, they reported in a subsequent study[40] that the largest uncertainties in pseudo-CT images still occur on the bone–tissue and air–tissue interfaces (400 HU). We have shown in this study that eddy currents can cause substantial errors in these regions, which can be corrected for using magnetic field monitoring. Another source of errors is geometrical distortions due to gradient nonlinearities, which can be compensated by geometrical correction methods[24,41,42] to improve coregistration of MR and PET images. It should be noted that these methods only correct for distortions caused by spatial nonlinearities in the gradient fields at edge of the field of view, which are static and do not account for dynamic trajectory errors from eddy currents.

PET simulation results show that misclassifications due to eddy currents can have substantial effects on the PET quantification, with oversegmentation of bone leading to a mean error in the uptake in the brain 9.16% when AC maps derived from nominal trajectories are used and errors of up to 12% in the SUV_{max} of the simulated lesions. In future work we plan to investigate the clinical impact of our eddy current correction method by comparing PET images in patient datasets using MR based attenuation maps derived using nominal and measured trajectories with CT based attenuation correction.

An advantage of using field monitoring for eddy-current correction is that a one-time calibration scan can be performed and the measured trajectories can be used in all subsequent image reconstructions for the same set of scan parameters. For the purposes of attenuation correction, it is likely to be acceptable to maintain the same scan parameters for each patient and so the calibration scan should not need to be repeated. It should be noted that as distortion of k-space trajectories leads to a mismapping of spatial frequencies during reconstruction, the appearance of the artifacts depends in part on the imaged object (or conversely its spatial frequency content). However, the trajectory distortions are due mainly to eddy currents induced in the scanner components and so are largely independent of the imaged object.

In this study the effect of improved UTE image reconstruction on segmented attenuation maps was demonstrated.

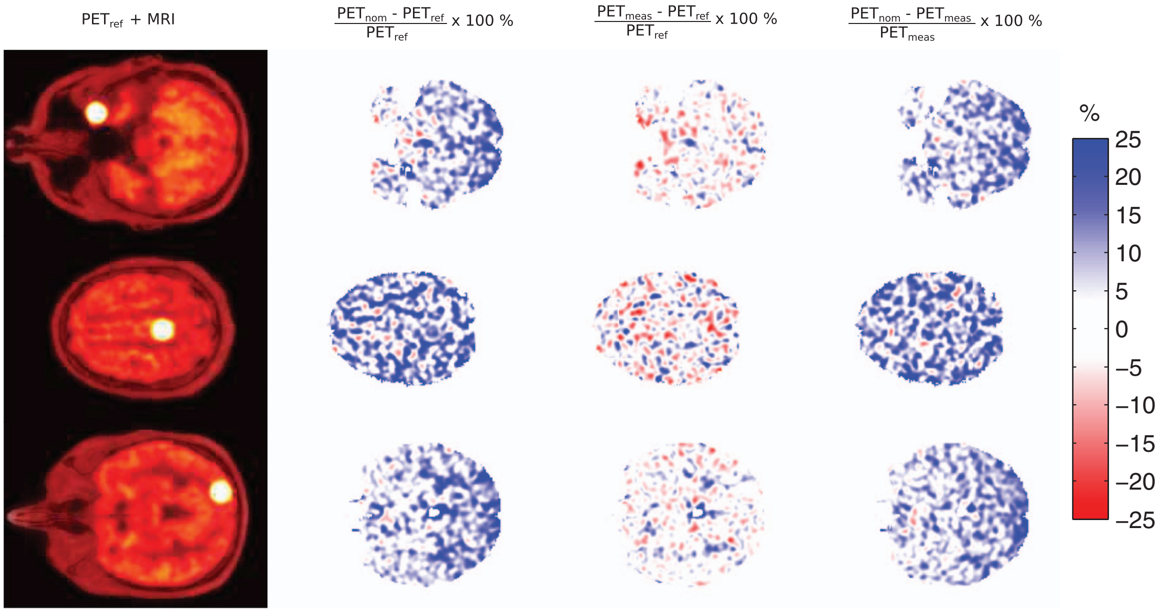

FIG. 10. Three axial slices containing lesions from PET simulation. From left to right: PET_{ref} images superimposed on MR echo image derived using measured trajectories. Relative (%) difference between PET_{nom} and PET_{ref}. Relative (%) difference between PET_{meas} and PET_{ref}. Relative (%) difference between PET_{nom} and PET_{meas}. Difference images are masked using a brain mask derived from the segmented emission map.

However, these methods could also be applied to other techniques for attenuation correction using UTE. Similar dual-echo UTE pulse sequences are used by several authors in both segmentation-based methods[14–16] and methods in which pseudo-CT images are derived.[20,40] Magnetic field monitoring could be applied to any of these sequences, or to the more complex triple-echo sequence proposed by Berker *et al.*[13] It could also be applied to MR-based radiotherapy treatment planning.

5. CONCLUSION

We have demonstrated that artifacts due to eddy currents in UTE MR imaging can lead to misclassification of tissue in segmented MR-based PET attenuation maps. We have shown that these artifacts can be corrected for by measuring the true k-space trajectories with a dynamic magnetic field camera and using these trajectories in the MR reconstruction. Results were demonstrated for a numerical simulation, for tissue phantom imaging and for *in vivo* cranial imaging of healthy volunteers. Further work is required to demonstrate the clinical impact of our method.

ACKNOWLEDGMENTS

The Ph.D.-studentship of A.P.A. is funded by Philips Healthcare. The authors acknowledge additional financial support from: (1) SUBLIMA project supported by the European Union under the seventh framework program (Grant No. 241711), (2) The Centre of Excellence in Medical Engineering funded by the Wellcome Trust and EPSRC (WT 088641/Z/09/Z), and (3) the Department of Health via the National Institute for Health Research (NIHR) comprehensive Biomedical Research Centre award to Guy's and St Thomas' NHS Foundation Trust in partnership with King's College London and King's College Hospital NHS Foundation Trust. The views expressed are those of the authors and not necessarily those of the NHS, the NIHR, or the Department of Health. The Image Registration Toolkit was used under Licence from Ixico Ltd.

[a] Also at Institute for Biomedical Engineering, University and ETH Zurich, Zurich 8092, Switzerland.

[b] Author to whom correspondence should be addressed. Electronic mail: Tobias.Schaeffter@kcl.ac.uk

[1] A. Drzezga, M. Souvatzoglou, M. Eiber, A. J. Beer, S. Fürst, A. Martinez-Möller, S. G. Nekolla, S. Ziegler, C. Ganter, E. J. Rummeny, and M. Schwaiger, "First clinical experience with integrated whole-body PET/MR: Comparison to PET/CT in patients with oncologic diagnoses," J. Nucl. Med. **53**, 845–855 (2012).

[2] C. Buerger, C. Tsoumpas, A. Aitken, A. P. King, P. Schleyer, V. Schulz, P. K. Marsden, and T. Schaeffter, "Investigation of MR-based attenuation correction and motion compensation for hybrid PET/MR," IEEE Trans. Nucl. Sci. **59**, 1967–1976 (2012).

[3] B. Guérin, S. Cho, S. Y. Chun, X. Zhu, N. M. Alpert, G. El Fakhri, T. Reese, and C. Catana, "Nonrigid PET motion compensation in the lower abdomen using simultaneous tagged-MRI and PET imaging," Med. Phys. **38**, 3025–3038 (2011).

[4] V. Keereman, P. Mollet, Y. Berker, V. Schulz, and S. Vandenberghe, "Challenges and current methods for attenuation correction in PET/MR," MAGMA (N.Y.) **26**, 81–98 (2013).

[5] G. Wagenknecht, H.-J. Kaiser, F. M. Mottaghy, and H. Herzog, "MRI for attenuation correction in PET: Methods and challenges," MAGMA (N.Y.) **26**, 99–113 (2013).

[6] A. Martinez-Möller, M. Souvatzoglou, G. Delso, R. A. Bundschuh, C. Chef D'Hotel, S. I. Ziegler, N. Navab, M. Schwaiger, and S. G. Nekolla, "Tissue classification as a potential approach for attenuation correction in whole-body PET/MRI: Evaluation with PET/CT data," J. Nucl. Med. **50**, 520–526 (2009).

[7] P. E. Kinahan, D. W. Townsend, T. Beyer, and D. Sashin, "Attenuation correction for a combined 3D PET/CT scanner," Med. Phys. **25**, 2046–2053 (1998).

[8] M. Hofmann, F. Steinke, V. Scheel, G. Charpiat, J. Farquhar, P. Aschoff, M. Brady, B. Scholkopf, and B. J. Pichler, "MRI-based attenuation correction for PET/MRI: A novel approach combining pattern recognition and atlas registration," J. Nucl. Med. **49**, 1875–1883 (2008).

[9] E. Rota Kops and H. Herzog, "Alternative methods for attenuation correction for PET images in MR-PET scanners," IEEE Nucl. Sci. Symp. Conf. Rec. **6**, 4327–4330 (2007).

[10] E. Rota Kops and H. Herzog, "Template based Attenuation Correction for PET in MR-PET Scanners," IEEE Nucl. Sci. Symp. Conf. Rec. **1**, 3786–3789 (2008).

[11] I. B. Malone, R. E. Ansorge, G. B. Williams, P. J. Nestor, T. A. Carpenter, and T. D. Fryer, "Attenuation correction methods suitable for brain imaging with a PET/MRI scanner: A comparison of tissue atlas and template attenuation map approaches," J. Nucl. Med. **52**, 1142–1149 (2011).

[12] E. Schreibmann, J. A. Nye, D. M. Schuster, D. R. Martin, J. Votaw, and T. Fox, "MR-based attenuation correction for hybrid PET-MR brain imaging systems using deformable image registration," Med. Phys. **37**, 2101–2109 (2010).

[13] Y. Berker, J. Franke, M. Palmowski, H. C. W. Donker, Y. Temur, F. M. Mottaghy, C. Kuhl, D. Izquierdo-Garcia, Z. A. Fayad, F. Kiessling, and V. Schulz, "MRI-based attenuation correction for hybrid PET/MRI systems: A 4-class tissue segmentation technique using a combined ultrashort-echo-time/dixon MRI sequence," J. Nucl. Med. **53**, 796–804 (2012).

[14] C. Catana, A. van der Kouwe, T. Benner, C. J. Michel, M. Hamm, M. Fenchel, B. Fischl, B. Rosen, M. Schmand, and A. G. Sorensen, "Toward Implementing an MRI-based PET attenuation-correction method for neurologic studies on the MR-PET brain prototype," J. Nucl. Med. **51**, 1431–1438 (2010).

[15] V. Keereman, Y. Fierens, T. Broux, Y. De Deene, M. Lonneux, and S. Vandenberghe, "MRI-based attenuation correction for PET/MRI using ultrashort echo time sequences," J. Nucl. Med. **51**, 812–818 (2010).

[16] A. Santos Ribeiro, E. Rota Kops, H. Herzog, and P. Almeida, "Skull segmentation of UTE MR images by probabilistic neural network for attenuation correction in PET/MR," Nucl. Instrum. Methods Phys. Res. A **702**, 114–116 (2013).

[17] G. Wagenknecht, E. R. Kops, L. Tellmann, and H. Herzog, "Knowledge-based segmentation of attenuation-relevant regions of the head in T1-weighted MR images for attenuation correction in MR/PET systems," IEEE Nucl. Sci. Symp. Conf. Rec. **1**, 3338–3343 (2009).

[18] H. Zaidi, M. L. Montandon, and D. O. Slosman, "Magnetic resonance imaging-guided attenuation and scatter corrections in three-dimensional brain positron emission tomography," Med. Phys. **30**, 937–948 (2003).

[19] A. Johansson, M. Karlsson, and T. Nyholm, "CT substitute derived from MRI sequences with ultrashort echo time," Med. Phys. **38**, 2708–2714 (2011).

[20] B. K. Navalpakkam, H. Braun, T. Kuwert, and H. H. Quick, "Magnetic resonance-based attenuation correction for PET/MR hybrid imaging using continuous valued attenuation maps," Invest. Radiol. **48**, 323–332 (2013).

[21] I. L. H. Reichert, M. D. Robson, P. D. Gatehouse, T. He, K. E. Chappell, J. Holmes, S. Girgis, and G. M. Bydder, "Magnetic resonance imaging of cortical bone with ultrashort TE pulse sequences," Magn. Reson. Imaging **23**, 611–618 (2005).

[22] D. C. Peters, J. A. Derbyshire, and E. R. McVeigh, "Centering the projection reconstruction trajectory: Reducing gradient delay errors," Magn. Reson. Med. **50**, 1–6 (2003).

[23] I. C. Atkinson, A. Lu, and K. R. Thulborn, "Characterization and correction of system delays and eddy currents for MR imaging with ultrashort echo-time and time-varying gradients," Magn. Reson. Med. **62**, 532–537 (2009).

[24] V. Rasche, D. Holz, and R. Proksa, "MR fluoroscopy using projection reconstruction multi-gradient-echo (prMGE) MRI," Magn. Reson. Med. **42**, 324–334 (1999).

[25] C. Barmet, N. De Zanche, and K. P. Pruessmann, "Spatiotemporal magnetic field monitoring for MR," Magn. Reson. Med. **60**, 187–197 (2008).

[26] G. F. Mason, T. Harshbarger, H. P. Hetherington, Y. Zhang, G. M. Pohost, and D. B. Twieg, "A Method to measure arbitrary k-space trajectories for rapid MR imaging," Magn. Reson. Med. **38**, 492–496 (1997).

[27] B. J. Wilm, C. Barmet, M. Pavan, and K. P. Pruessmann, "Higher order reconstruction for MRI in the presence of spatiotemporal field perturbations," Magn. Reson. Med. **65**, 1690–1701 (2011).

[28] D. Giese, M. Haeberlin, C. Barmet, K. P. Pruessmann, T. Schaeffter, and S. Kozerke, "Analysis and correction of background velocity offsets in phase-contrast flow measurements using magnetic field monitoring," Magn. Reson. Med. **67**, 1294–1302 (2012).

[29] L. Greengard and J. Y. Lee, "Accelerating the nonuniform fast Fourier transform," SIAM Rev. **46**, 443–454 (2004).

[30] N. R. Zwart, K. O. Johnson, and J. G. Pipe, "Efficient sample density estimation by combining gridding and an optimized kernel," Magn. Reson. Med. **67**, 701–710 (2012).

[31] E. N. Yeh, M. Stuber, C. A. McKenzie, R. M. Botnar, T. Leiner, M. A. Ohliger, A. K. Grant, J. D. Willig-Onwuachi, and D. K. Sodickson, "Inherently self-calibrating non-Cartesian parallel imaging," Magn. Reson. Med. **54**, 1–8 (2005).

[32] K. P. Pruessmann, M. Weiger, P. Börnert, and P. Boesiger, "Advances in sensitivity encoding with arbitrary k-space trajectories," Magn. Reson. Med. **46**, 638–651 (2001).

[33] C. Barmet, N. De Zanche, B. J. Wilm, and K. P. Pruessmann, "A transmit/receive system for magnetic field monitoring of *in vivo* MRI," Magn. Reson. Med. **62**, 269–276 (2009).

[34] L. R. Dice, "Measures of the amount of ecologic association between species," Ecology **26**, 297–302 (1945).

[35] C. Studholme, D. L. G. Hill, and D. J. Hawkes, "An overlap invariant entropy measure of 3D medical image alignment," Pattern Recogn. **32**, 71–86 (1999).

[36] B. Aubert-Broche, A. C. Evans, and L. Collins, "A new improved version of the realistic digital brain phantom," NeuroImage **32**, 138–145 (2006).

[37] C. Tsoumpas, C. Buerger, A. P. King, P. Mollet, V. Keereman, S. Vandenberghe, V. Schulz, P. Schleyer, T. Schaeffter, and P. K. Marsden, "Fast generation of 4D PET-MR data from real dynamic MR acquisitions," Phys. Med. Biol. **56**, 6597–6613 (2011).

[38] C. Tsoumpas, P. Aguiar, K. S. Nikita, D. Ros, and K. Thielemans, "Evaluation of the single scatter simulation algorithm implemented in the STIR library," IEEE Nucl. Sci. Symp. Conf. Rec. **6**, 3361–3365 (2004).

[39] K. Thielemans, C. Tsoumpas, S. Mustafovic, T. Beisel, P. Aguiar, N. Dikaios, and M. W. Jacobson, "STIR: Software for tomographic image reconstruction release 2," Phys. Med. Biol. **57**, 867–883 (2012).

[40] A. Johansson, M. Karlsson, J. Yu, T. Asklund, and T. Nyholm, "Voxel-wise uncertainty in CT substitute derived from MRI," Med. Phys. **39**, 3283–3290 (2012).

[41] S. J. Doran, L. Charles-Edwards, S. A. Reinsberg, and M. O. Leach, "A complete distortion correction for MR images: I. Gradient warp correction," Phys. Med. Biol. **50**, 1343–1361 (2005).

[42] C. P. Karger, A. Höss, R. Bendl, V. Canda, and L. Schad, "Accuracy of device-specific 2D and 3D image distortion correction algorithms for magnetic resonance imaging of the head provided by a manufacturer," Phys. Med. Biol. **51**, N253–N261 (2006).

[43] See supplementary material at http://dx.doi.org/10.1118/1.4837315 for Figs. S1–S3.